Worming Their Way into Shape: Toroidal Formations in Micellar Solutions

Joshua J. Cardiel,[†] Lige Tonggu,[‡] Alice C. Dohnalkova,[§] Pablo de la Iglesia,[⊥] Danilo C. Pozzo,[⊥] Liguo Wang,[‡] and Amy Q. Shen[†,*]

[†]Department of Mechanical Engineering and [‡]Department of Biological Structure, University of Washington, Seattle, Washington 98195, United States, [§]Environmental Molecular Sciences Laboratory, Pacific Northwest National Laboratory, Richland, Washington 99354, United States, and [⊥]Department of Chemical Engineering, University of Washington, Seattle, Washington 98195, United States

ABSTRACT

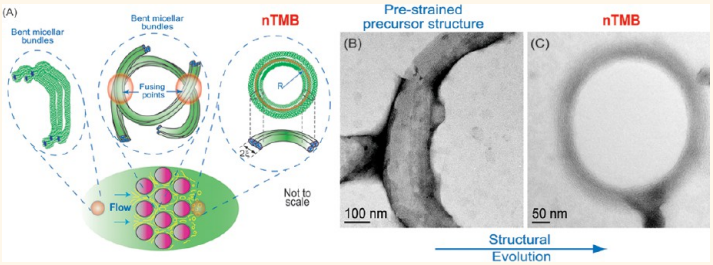

We report the formation of nanostructured toroidal micellar bundles (nTMB) from a semidilute wormlike micellar solution, evidenced by both cryogenic-electron microscopy and transmission electron microscopy images. Our strategy for creating nTMB involves a two-step protocol consisting of a simple prestraining process followed by flow through a microfluidic device containing an array of microposts, producing strain rates in the wormlike micelles on the order of 10^5 s^{-1}. In combination with microfluidic confinement, these unusually large strain rates allow for the formation of stable nTMB. Electron microscopy images reveal a variety of nTMB morphologies and provide the size distribution of the nTMB. Small-angle neutron scattering indicates the underlying microstructural transition from wormlike micelles to nTMB. We also show that other flow-induced approaches such as sonication can induce and control the emergence of onion-like and nTMB structures, which may provide a useful tool for nanotemplating.

KEYWORDS: toroidal nanostructures · wormlike micelles · flow-induced structures · microfluidics · sonication

Self-assembled nanostructures can exist in various morphologies such as spherical micelles, cylindrical micelles, vesicles, bilayers, tubes, and toroids. Among them, toroidal structures possess unique annular shapes and materials properties, serving as a good model system for nanotemplating and biomolecule encapsulations.[1−4] Even though toroidal nanostructures have been formed in surfactants,[5] block copolymers,[6,7] and other self-assembly systems,[8,9] the high-throughput synthesis of toroidal nanostructures with reproducible shape and dimensions has been a key challenge for further exploring their applications. Flow-induced synthesis approach is a promising candidate for scaled-up nanomaterial production with desirable properties. For example, Wang *et al.*[10] reported a new strategy to generate a large amount of micrometer size toroidal particles through solidification of polymer droplets in a microfluidic device. However, the flow-induced nanotoroid formation has not previously been investigated.

In this work, we report a flow-induced, guided-assembly process to produce stable nanostructured toroidal micellar bundles (nTMB) in a semidilute wormlike micellar solution (precursor) with low surfactant and salt concentrations. Wormlike micelles are elongated and flexible cylindrical aggregates with radii around 1−3 nm with lengths that may vary from nanometers to micrometers. The properties of wormlike micelles are similar to those of conventional flexible polymers.[11,12] However, wormlike micelles can break and recombine in response to changes of ionic strength, temperature, and

* Address correspondence to amyshen@uw.edu.

Received for review May 30, 2013 and accepted October 29, 2013.

Published online October 29, 2013
10.1021/nn404191s

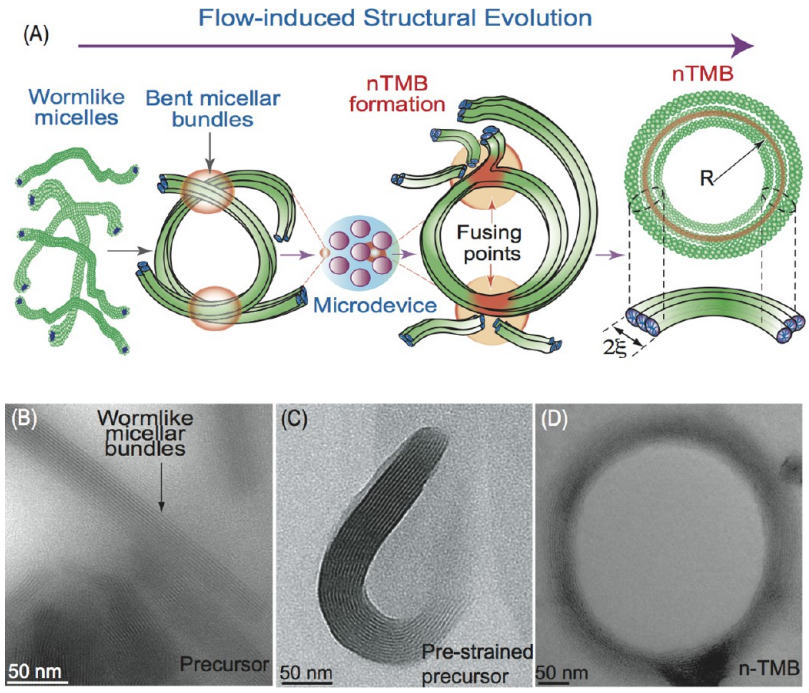

Figure 1. (A) Schematic of the microstructural evolution from wormlike micellar bundles to nTMB. When two flexible wormlike micellar bundles are brought together, they fuse at their cylindrical parts, creating a nTMB. The red circle in the schematic of the nTMB represents its neutral axis. (B) TEM image of the precursor, showing a mixture of wormlike micelles and micellar bundles. (C) TEM images of a precursor that was prestrained at $\dot{\gamma}_{ps} \approx 6.7 \times 10^4\ s^{-1}$, showing bent micellar bundles. (D) TEM image of a nTMB.

flow conditions.[12] Clausen *et al.*[14] were one of the first groups to report the formation of micellar torii in a wormlike micellar solution. Working with a solution consisting of the ionic surfactant CTAC, the inorganic salt NaCl, and the organic salt NaSal, they fixed the molar concentration of CTAC (0.05 M) and NaCl (0.1 M) while varying the molar ratio NaSal/(CTAC-NaCl) from 0 to 2.0 and observed toroidal micelles at a molar ratio of 1.0. In *et al.*[5] observed irregular and amorphous closed-looped micelles in a cationic surfactant tetramer solution. They found the size distribution of these micelles with respect to contour length to be monomodal, with a distribution peak around 150 nm. Gummel *et al.*[15] inferred the existence of torii in an anionic and zwitterionic surfactant solution from small-angle X-ray scattering (SAXS) patterns by fitting the scattering spectra to a toroidal form factor and deduced the thickness of toroidal micelles (~10 nm) with elliptical cross section. They proposed that wormlike micelles may close off to form torii if the micellar length reaches a critical value. Cates and Candau[16] suggested that micellar rings may induce shear thickening behavior in micellar solutions. They proposed that shear thickening behavior might be caused by the interlinking and delinking of large micellar rings in a process requiring a positive feedback between the strain applied and the linking−delinking of the rings. Padding and Boek[17] used non-equilibrium molecular dynamics simulations to predict that, at fixed micellar concentration, shear flow may induce the formation of rings from wormlike micelles. They found that shear flow would decrease the entropy gain of the system and promote the formation of micellar rings.

The Helfrich curvature free-energy model and the Poisson−Boltzmann equation have been frequently used to describe the formation, stability, and mechanical properties of membranes, vesicles, and toroidal structures.[18−21] For example, Sakaue[19] used Monte Carlo simulations to capture the formation of multiple torii from weakly charged wormlike chains, finding that, for weakly charged wormlike chains, the thickness of the torus is dictated by the surface energy and bending modulus of the chains. He and Schmid[22] performed mesoscopic field-based simulations to predict complex nanostructured micellar structural formations (*e.g.*, toroidal micelles) in an amphiphilic block copolymer solution, concluding that toroidal micelles may be formed by controlling the copolymer volume fraction, molecular packing parameters, and kinetic segregation in the solution.

Recently,[23] we reported the formation of highly entangled and multiconnected networks of micellar bundles when a semidilute wormlike micellar solution (precursor) with low surfactant and salt concentrations was pumped through a microfluidic device containing hexagonal micropost arrays. In the work described here, we employed a two-step protocol wherein the same precursor is prestrained and then pumped into a microdevice identical to that used in our previous work[23] (see schematics in Figure 1A). In combination with microfluidic confinement, these unusually large

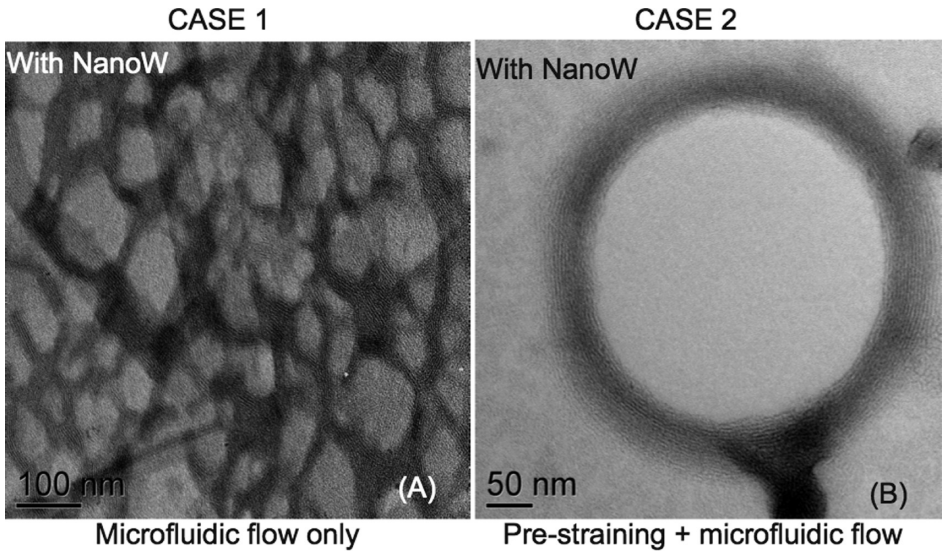

Figure 2. Structure comparison with and without prestraining treatment. (A) TEM image of the microstructure formed by using microfluidics.[23] (B) TEM image of the microstructure formed by combining the prestraining process and microfludics.

strain rates allow for the formation of stable nanostructured toroidal micellar bundles (nTMB). To examine the structure of the nTMB, we used a combination of cryogenic-electron microscopy (cryo-EM), transmission electron microscopy (TEM) imaging, and small-angle neutron scattering (SANS) characterizations. In particular, systematic TEM was applied to over 300 nTMBs from different samples to obtain the size distribution of toroidal radius R, as measured from the center to the neutral axis of the nTMB. SANS measurements were used to characterize the structural transition from the precursor to nTMB. We also observed that nTMB remained stable at room temperature for no less than 5 days. Possible mechanism for the nTMB formation is proposed. Our work demonstrates that flow-induced approach is a promising candidate for scaled-up nanomaterial synthesis with desirable morphologies and properties.

RESULTS AND DISCUSSION

Our semidilute wormlike micellar aqueous solution (precursor) consists of cetyltrimethyl ammonium bromide ([CTAB] = 50 mM) and organic salt sodium salicylate ([NaSal] = 16 mM), with a molar ratio (NaSal/CTAB) of 0.32. A mini vortexer was used to prestrain the micellar solution at $\dot{\gamma}_{ps} \approx 6.7 \times 10^4\ s^{-1}$ for 15 s.[24] The prestrained solution was then immediately pumped through the microdevice at a constant flow rate of 15 mL/h (see Figure 1A). We used a PDMS−glass microdevice containing a hexagonal array of microposts with a diameter of 100 μm, a height of 75 μm, and a micropost gap size of 15 μm (see Experimental Section for fabrication details). For the given flow rate and channel dimensions, we estimated the maximum rate of strain in the microdevice to be $\dot{\gamma}_{microdevice} \approx 4.4 \times 10^4\ s^{-1}$.[25] The total strain rate that induces the nanostructured toroidal micellar bundle (nTMB) formation is then $\dot{\gamma}_{total} \approx 1.1 \times 10^5\ s^{-1}$. The formation of nTMB appears to be strongly dependent on the prestraining process. A large quantity of nTMBs formed for a critical prestrain rate of $\dot{\gamma}_{ps} \approx 6.7 \times 10^4\ s^{-1}$ in the wormlike micellar solution, followed by passing the solution to the micropost arrays (Figure 6A). In contrast, at a lower prestrain rate of $\dot{\gamma}_{ps} \approx 3.5 \times 10^4\ s^{-1}$, only bent micellar bundles (Figure 1C and Figure 4) were observed. When the prestraining step was absent, we only observed highly branched and entangled wormlike micellar bundles (see Figure 2). This result indicates that the flow procedure difference is the key to form nTMB.

Cryogenic-electron microscopy and transmission electron microscopy using a Tecnai G2 F20 (FEI Co., Hillsboro, OR) at 200 kV were both conducted to image the precursor, prestrained precursor, and nTMB. The electron dose ranged from 1000 to 3000 electrons/nm^2. Cryo-EM imaging is desirable because it can capture the true microstructure of a given sample in its native hydrated environment, especially for surfactant and lipid systems.[46] However, the resolution of cryo-EM tends to be sacrificed with the vitreous ice layer on the sample. Taking these factors into consideration, we performed both TEM and cryo-EM imaging of the nTMBs for comparison purposes, shown in Figure 3 and Figure 10 in the Experimental Section.

Figure 3 shows various nTMBs obtained by cryo-EM, without negative stain NanoW. After producing the nTMBs *via* the microfluidics device, we immediately prepared the cryo-EM sample by a freeze-plunging method (more details in Experimental Section) and waited for 24 h before imaging to remove any ethane left on the TEM grid. The radius of the nTMBs ranges between 16 and 198 nm with a thickness of ~24 ± 9 nm. Since the morphological comparison of gradually

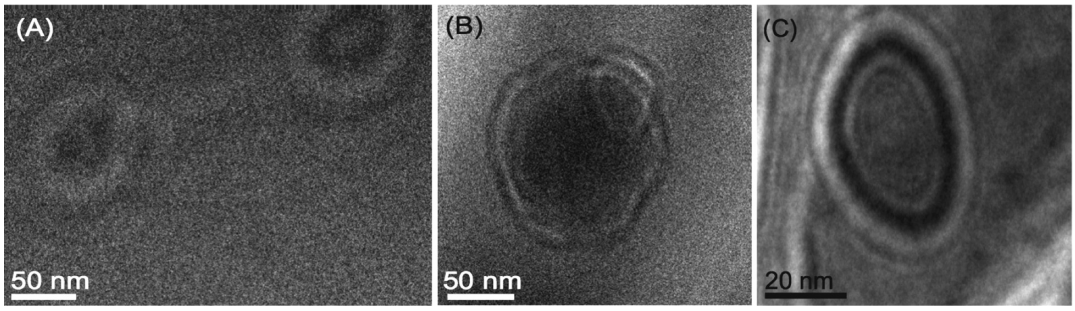

Figure 3. Cryo-EM images of the nTMB without negative stains. The thickness of the bundles is ~18 ± 4 nm.

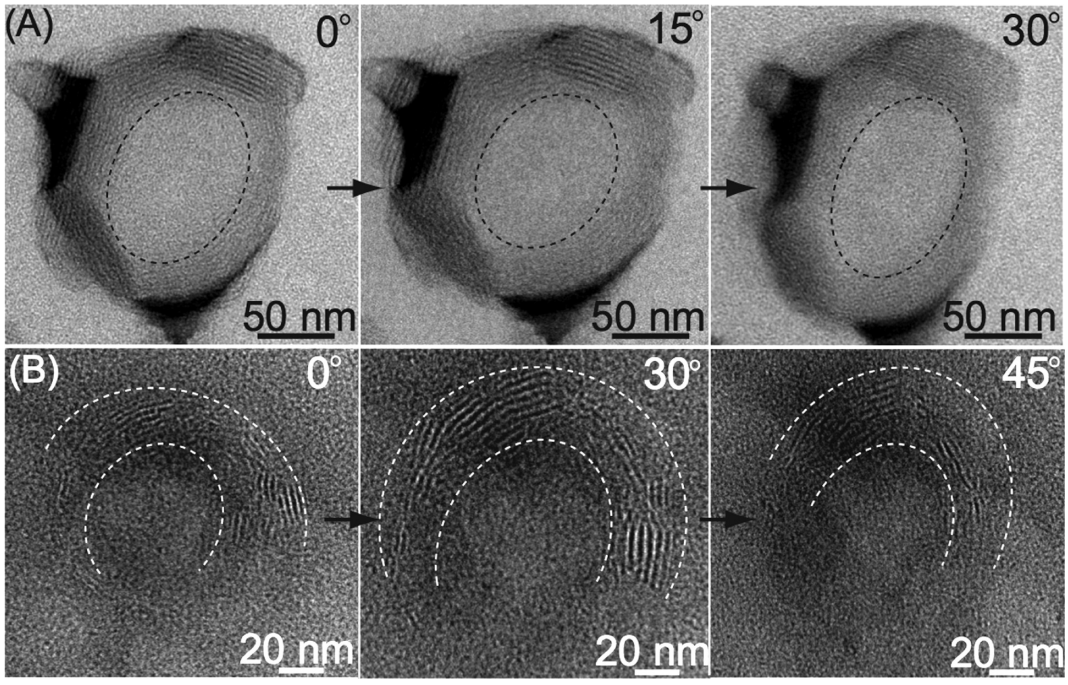

Figure 4. nTMB tilted at different angles. (A) nTMB created at $\dot{\gamma}_{ps} \approx 6.7 \times 10^4$ s^{-1} with the prestraining process. The diameter of the nTMB varies up to 15% when tilted in the direction perpendicular to the tilt axis (0 to 30°), indicating planarity. (B) Semicomplete nTMB created at $\dot{\gamma}_{ps} \approx 3.5 \times 10^4$ s^{-1} with the prestraining process. The diameter and the shape of the semicomplete nTMB change with varying tilt angles, verifying the two-dimensionality of the structures. White dashed and black dashed lines are guide lines.

air-dried and frozen but hydrated samples by TEM and cryo-EM has shown excellent ultrastructural correlation in both methods (more details in Experimental Section), to avoid the decreased resolution caused by imaging through the vitreous ice layer with cryo-EM, we proceeded with room temperature TEM imaging with negative stain NanoW for the following discussions related to nTMBs.

In the precursor solution, we observed a mixture of elongated and dispersed micellar bundles and single wormlike micelles (Figure 1B). The micellar bundles had thickness and length of approximately 50 ± 16 nm and 800 ± 125 nm, respectively; individual wormlike micelles showed a mean diameter and mean length of 5 and 16 nm, respectively, which is consistent with the literature.[12] Hence, each micellar bundle in the precursor consists of approximately 3−6 parallel wormlike micelles (Figure 1B). As Sal ions from NaSal reside at the interface of the wormlike micelle and water, the CTAB micellar core can be effectively neutralized to induce the bundle formation.[26−28] In the prestrained precursor, we observed elongated and bent micellar bundles (Figure 1C). The bent micellar bundles formed arc segments on the order of micrometers with similar bundle thickness as those shown in the precursor. The postflow sample shows the formation of nTMB, with an approximate bundle thickness of $2\xi \approx 24 \pm 9$ nm and radius R ranging from 16 to 198 nm (Figure 1D, Figure 4A, Figure 6A,B, and Figure 7A). Relative to bundles found in the precursor, the thickness of nTMB tends to be smaller and to have a wider size distribution.

To determine whether the nTMBs are two-dimensional or three-dimensional objects (*e.g.*, planar tori or vesicles), the samples were tilted at multiple angles

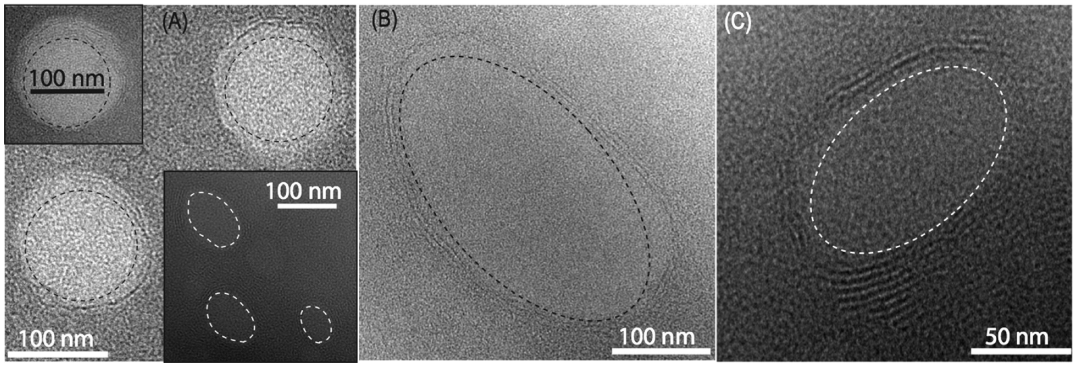

Figure 5. TEM images of the nTMBs that have been stored in DI water for 5 days. (A) Circular nTMBs and (B) elliptical nTMBs were observed in the stored samples. The thickness of the bundles is ~10−20 nm.

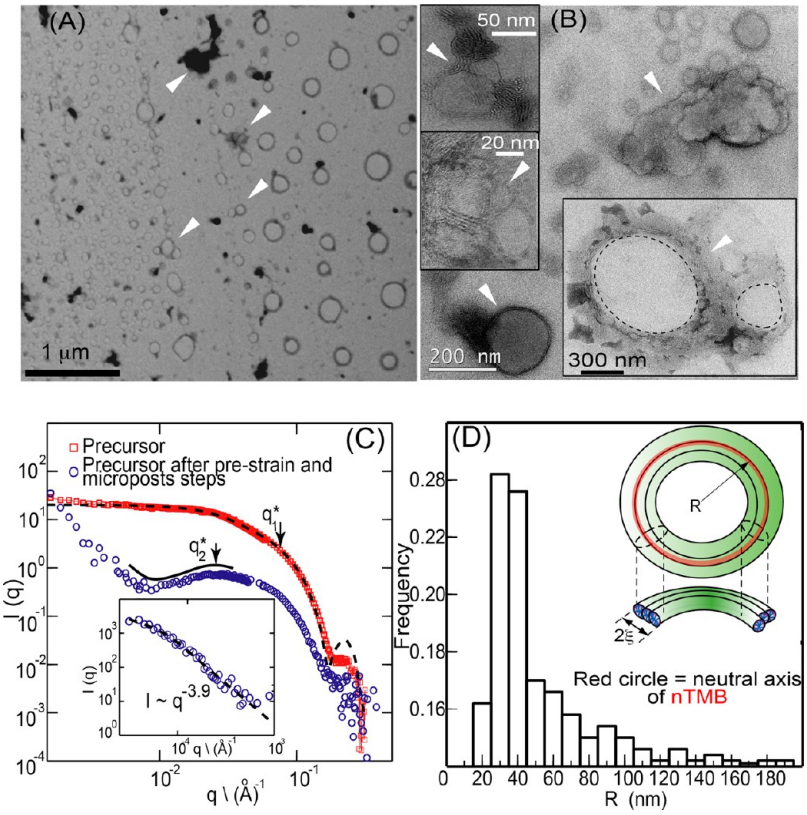

Figure 6. (A) TEM image of nTMBs with various sizes. (B) TEM images of interlinked nTMBs; the insets show the interlinkage of large and small nTMBs (white triangles). Black dashed lines are guide lines. (C) SANS spectra of the precursor and the postflow solution. The precursor (red squares) is fitted to a dispersed cylindrical micellar model (dashed black line) with a mean radius of 2.2 nm and a mean length of 16 nm. The SANS spectra of the postflow solution exhibit microstructural changes (blue circles) related to the formation of nTMB and larger micellar aggregates; the solid black line is a guide line to show the correlation peak in the SANS data ($q_2^* \approx 25.1$ nm); q_2^* is in good agreement with the thickness of the nTMB measured from TEM images ($\xi \approx 24 \pm 9$ nm). The inset shows the USANS spectra at low q with a power law dependence in the scattering intensity (fitted to a Guinier model). (D) nTMB size distribution of R.

before imaging (see Figure 4). A TEM image is the projection of a sample onto a two-dimensional plane. If the nTMB is three-dimensional, the diameter of the projection should not change when the structure is tilted. However, if the nTMB is two-dimensional, the diameter and the thickness of the projection of the nTMB, in the direction normal to the tilting axis, should change with the tilting angle. Since the diameter and thickness of both nTMB and bent micellar bundles at different tilting angles vary between 5 and 15% (see Figure 4), we infer that both the micellar bundles and the nTMB are two-dimensional planar structures. The nTMBs have been shown to be stable; we imaged nTMBs that were stored in DI water at room temperature for 5 days (see Figure 5).

A histogram of the radius R distribution of the nTMBs was constructed by measuring over 300 nTMBs from different TEM samples (see Figure 6D). We obtained a

mean radius $R \approx 68 \pm 37$ nm and a mean thickness $2\xi \approx 24 \pm 9$ nm. From the histogram, we observed that the dominant size of the nTMB ranged between 30 and 40 nm in radius. Jung *et al.*[29] studied the stability and formation of vesicles in a sodium perfluorooctanoate (FC_7)/CTAB vesicle solution at high salt concentrations, finding that the radius of the vesicles ranged between 23 and 37 nm.

Small-angle neutron scattering experiments were conducted at the National Institute of Standards and Technology Center for Neutron Research (NCNR) in Gaithersburg, Maryland. SANS was performed using a standard configuration to cover a wide range of wave vector values. In addition, ultra-small-angle neutron scattering (USANS) measurements were performed by using a perfect crystal diffractometer BT5 at the NCNR.[30] USANS increases the scattering range, so that submicrometer and micrometer sized features of the nTMB could also be probed. The SANS data of the precursor were fitted to a dispersed cylindrical micellar model.[31] From the data fit, the structures in the precursor were found to have a mean radius of approximately 2.2 nm (q_1^*) and a mean length of approximately 16 nm (red symbols in Figure 6C).[31] These dimensions are consistent with the size of single wormlike micelles reported in literature. Although our TEM images show a mixture of single wormlike micelles and micellar bundles in the precursor solution (Figure 1B), we suspect that single wormlike micelles outnumber micellar bundles in the precursor; the SANS measurements therefore captured only the dimensions of the single wormlike micelles present in the precursor solution.

The SANS data of the postflow solution (blue symbols in Figure 6C) differ significantly from that of the precursor. Due to the presence of individual wormlike micelles, wormlike micellar bundles, and nTMB, no currently available model can be acceptably fit to the SANS spectra. Nevertheless, we estimated some of the characteristic dimensions in the postflow sample. At intermediate values of the scattering vector (q_2^*), we found a correlation peak of ≈25 nm, which matches well with the thickness of the micellar bundles obtained from TEM images of nTMB ($2\xi \approx 24 \pm 9$ nm). At low values of the scattering vector ($q < q_2^*$), a power law dependence ($I \approx q^{-3.9}$) in the scattering intensity is observed (inset in Figure 6C) and is related to the presence of larger micellar structures. Using the Guinier model[31] to fit the SANS spectra at low q, we extracted a characteristic dimension of ≈1.1 μm in the postflow sample. In our TEM images, we noted the presence of some large aggregates as well as the interlinking nTMB (white triangles in Figure 6A,B) on the order of micrometers. Structures like these may generate complex scattering spectra which are difficult to fit. Still, SANS verifies the existence of a dramatic flow-induced structural transition consistent with our TEM and cryo-EM results.

The net free energy of a wormlike micelle includes contributions associated with bending of its centerline, electrostatic interactions, and the presence of end-caps. Closing a wormlike micelle eliminates the latter contribution but increases the remaining contributions and, thus, involves overcoming an energy barrier. An activation energy is therefore needed to form nTMBs. The necessary activation energy can be provided by tuning the thermodynamic properties of the micellar solution[5,14,15,22,32] or by subjecting the solution to flow.[17] We employ the second of these strategies *via* a prestraining process and flow through a specially designed microfluidic device containing micropost arrays. In the precursor, the penetration of Sal ions in the CTA core[26,27] enhances the flexibility of the wormlike micelles. During the prestraining process of the precursor, external energy input bends the flexible wormlike micelles. Subsequently, the presence of micropost arrays in our device enables local concentration gradients of the bent wormlike micelles[33,34] along with high extension and shear rates,[23,25,35] which promote high stretching of the wormlike micelles and wormlike micellar bundles. High stretching and flow alignment decrease the bending rigidity of the wormlike micellar bundles. The free energy of surfactant molecules in the end-cap therefore increases relative to the curvature energy of the cylindrical body of the micelle, leading to a decrease in the work required to form connections.[36] As adjacent and bent micellar bundles flow through the confined microposts, it becomes energetically favorable to minimize the number of end-caps while concurrently promoting the fusion of the bent micellar bundles, yielding nTMB (Figure 1A). Interlinked nTMBs (see white triangles in Figure 6A,B) were also evident in TEM images. The interlinkage of torus micelles has been related to the shear thickening behavior of micellar solutions.[16,17]

In the postflow sample, we also observed a wide variety of nTMB shapes: perfectly circular, polygon-like, noncircular, and semicomplete nanostructures (Figure 7). The diverse morphology of toroidal structures has also been reported for toroidal vesicles by tuning the temperature in the suspending solution.[32] The morphological diversity in our experiments originates from the lack of control of the energy input during the prestraining process. Our ongoing effort is to develop an optimal flow protocol to control the sizes and shapes of nTMB and possibly other micellar nanostructures. For example, a variety of interesting nanostructures were created when the precursor flows through the microdevice (no prestraining), followed by sonicating the sample at 42 kHz at 100 W. With no sonication, we observed highly entangled and multiconnected micellar bundle networks (Figure 8A).[23] At 5 min of sonication, dispersed onion-like micellar structures formed (Figure 8B). Diat *et al.* reported that shear flow could induce the transition from lamellar to onion-like structures in surfactant solutions.[37] At 10 min of sonication, elliptical torus-like micelles were observed (Figure 8C). At 15 min of sonication, nTMBs were observed. These nTMBs have a thickness of $\sim 10 \pm 5$ nm and a radius ranging from 20 to 30 nm (Figure 8D). The general trend

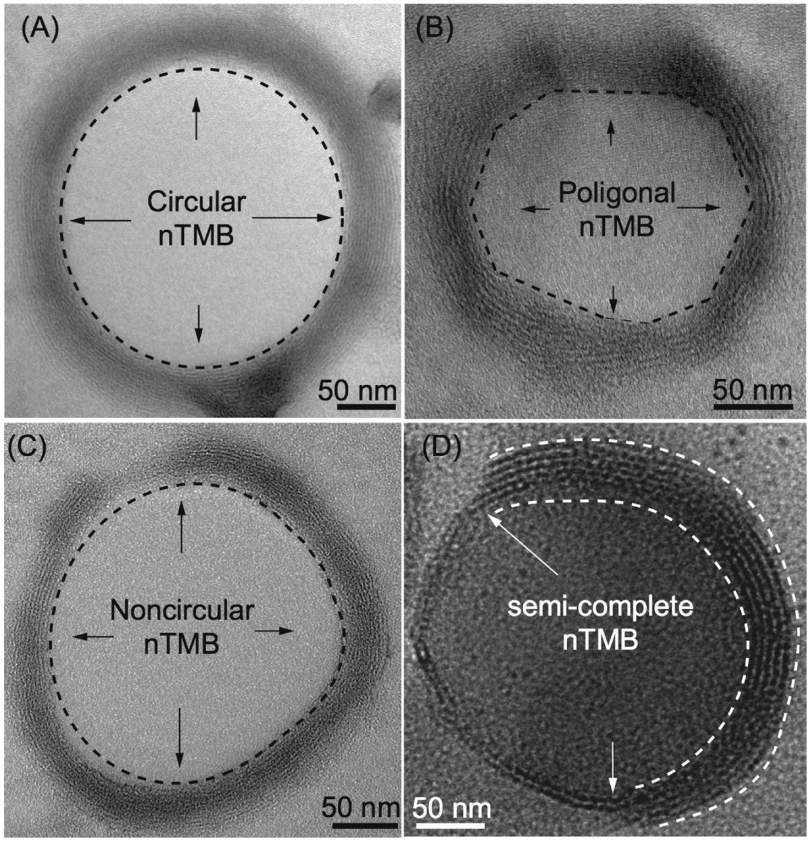

Figure 7. Diversity of nTMB. (A) Circular nTMB, (B) polygonal nTMB, (C) noncircular nTMB, and (D) incomplete semicircular nTMB. Circular nTMBs were the dominant structure observed in the TEM micrographs.

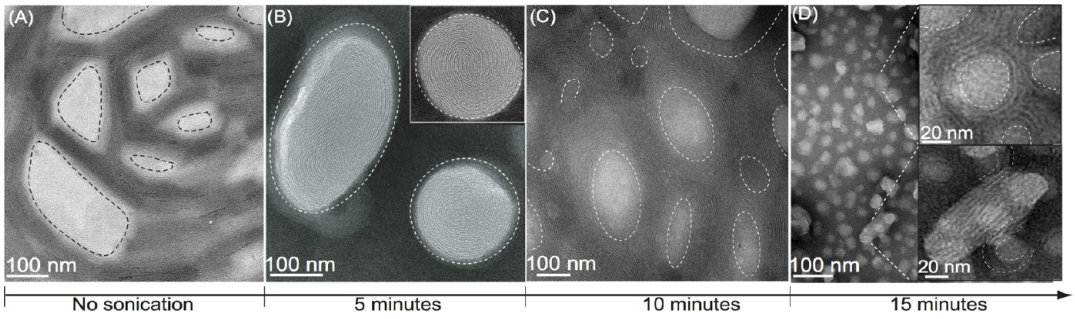

Figure 8. TEM images of the postflow solution (precursor through micropost arrays followed by sonication). The sonication was held at 42 kHz. (A) With no sonication, a highly entangled and multiconnected micellar bundle network is formed; the bright areas are pores in the micellar network, while the darkest regions are interconnected micellar bundles. (B) At 5 min of sonication, onion-shaped micellar structures formed. (C) At 10 min of sonication, ellipsoidal torus-like micelles formed. (D) At 15 min of sonication, regular sized nTMBs (~20−30 nm in diameter) are formed (see top inset); some micellar bundles coexist with the nTMB (see bottom inset). The lower inset shows the coiling of two wormlike micelles to form a nTMB (white dashed lines).

shows that the characteristic dimensions of the observed nanosized micellar structures decrease with increasing sonication time. Yusof *et al.*[38] studied the effects of sonication (211 kHz) in a wormlike micellar solution consisting of [CTAB] = 0.015 M and [NaSal] = 0.015 M. They reported the formation of long threadlike micelles and multiconnected tubular micelles, but they did not observe toroidal structures. These preliminary studies indicate that the flow procedure and the kinematics of the flow are critical to the structural formation in wormlike micelles.

CONCLUSION

We report a simple flow-induced procedure (prestraining process with microfluidic flow) to generate nanostructured toroidal micellar bundles (nTMB) in a semidilute micellar solution (CTAB/NaSal). These nTMBs, which consist of regular sized and shaped micellar bundles, were found to form at low salt concentrations and to remain stable for no less than 5 days. The dimensions of the nTMBs were visualized by TEM and cryo-EM imagings and are consistent with the structural

transition trend illustrated by SANS measurements. These nanostructured toroidal micellar bundles provide a potential platform as nanoreactors, encapsulation and drug carriers with tunable shapes, sizes, and structural rigidities. We also showed that other flow-induced approaches such as sonication could generate and control the emergence of onion-shaped and nanotoroidal structures that are useful for nanotemplating. Finally, our work demonstrates that the flow-induced approach is a promising candidate for scaled-up nanomaterial synthesis with desirable properties.

EXPERIMENTAL SECTION

Precursor Preparation. Semidilute micellar solution (precursor) was used to form the nanostructured toroids. The micellar solution is a mixture of DI water with surfactant CTAB (Sigma Aldrich Co.) and organic salt NaSal (Sigma Aldrich Co.). The solutions were prepared by adding the appropriate amounts of CTAB and NaSal to DI water and mixing for at least 4 h using a magnetic stir bar, and then left at rest for 2 days to equilibrate under room temperature. For microrheology, the precursor solutions were also seeded with 1 μm diameter polystyrene probe particles (Thermo Scientific) with 0.01 wt %. A mini vortexer (Fisher Scientific) was used to prestrain the micellar solution at ~53.0 rad/s for 15 s. The prestrained solution was then immediately pumped through a microdevice at a constant flow rate of 15 mL/h.

Microfluidic Device Fabrication. The devices were fabricated using standard soft lithography techniques.[4,39] Briefly, a thin layer of SU-8 2035 photoresist (MicroChem Corp., Newton, MA) was spun onto a silicon wafer and cured. A Heidelberg μPG-101 machine (Heildelberg Instruments GmbH, Heildelberg, 45 Germany) at 4× speed and 75% of 18 mW was applied to write the mold of microchannel onto the photoresist. The wafer was subsequently cured, developed, and surface treated to ensure it is hydrophobic. Modeling glue sticks the silicone tubing ports at the designed inlets and outlets of the microchannel. A mixure 10:1 of Sylgard 184-PDMS elastomer was poured onto the model wafer, desiccated, and cured at 60 °C for ~1 h. The resulting PDMS cast was peeled off the wafer and plasma bonded onto a glass slide using a Femto plasma cleaner (Diener Electronic). A syringe pump (Harvard apparatus) was used to pump the precursor solution into the device through the inserted polyethylene tubing (Intramedic). The PDMS−glass microfluidic device has a channel height of 75 μm, containing a hexagonal array of microposts with a diameter of 100 μm and a spacing of 15 μm.

Bulk Shear Rheometry. Steady shear rheometry and oscillatory shear rheometry were performed using a stress controlled rheometer (AR 2000) on the precursor solution. The temperature was fixed at 23 °C, and a solvent trap was used to avoid evaporation. An acrylic cone−plate geometry (40 mm in diameter and 2° of truncation angle) was used for all measurements. Figure 9 shows the shear viscosity of the precursor as a function of the shear rate. The precursor solution exhibited a distinct viscosity jump once a critical shear rate was reached ($\dot{\gamma}_c \sim 25\ s^{-1}$). The increment in the apparent viscosity has been attributed to the formation of transient shear-induced structures created by entangled wormlike micellar networks under shear flow.[12] When the shear rate increased further ($\dot{\gamma} \sim 100\ s^{-1}$), the wormlike micelles would align in the flow direction, leading to a viscosity drop.

Oscillatory shear experiments were conducted at several strains to ensure the linear viscoelastic regime. The viscoelasticity behavior in the precursor was correlated with a Maxwellian relationship with a single-dominant relaxation time. This stress relaxation time λ can be extracted from the first crossover between the viscous modulus (G'') and the elastic modulus (G'). The Maxwell model can also deduce G_0, a value at which the elastic modulus G' reaches a plateau at high frequencies. The range of frequencies was varied from 0.01 to 100 Hz. Note that our stress-controlled rheometer is not sensitive enough to extract λ for the precursor solution due to its weakly viscoelastic nature. Hence, microrheometry was used as an alternative to obtain λ and G_0 for the precursor (see below). The inset in Figure 9 shows good agreement between the bulk rheometry and the microrheometry of the precursor within the ω limit from the bulk rheometry.

Microrheometry. Using standard microrheology procedures,[42] the precursor solution was seeded with micrometer size probe particles at 0.01 wt %. An area of ≈1000 μm^2 was selected for video microscopy. Videos were recorded at magnifications of 150× using a Leica DMR-IRB inverted microscope (PI Floutar 100×/1.30 NA oil objective with 1.5 tube lens). The videos consisting of 8192 frames were taken at 125 frames per second (fps) with a high-speed camera (Photron FASTCAM). We performed passive microrheology on the precursor.[40−42] The two-dimensional mean-square displacement (msd = $\langle \Delta r^2(t) \rangle$) of the embedded microbeads in the precursor was calculated. Some light smoothing using a moving average filter (windows size of 51 frames) was performed on the MSD data prior to further analysis. The msd was then related to the complex modulus $G^*(\omega)$ of the precursor. The complex modulus comes from the Stokes−Einstein relation described in Mason.[41] This relation shows that the shear stress relaxation in the locality of the particle is identical to that of the bulk fluid subjected to a shear strain. The complex modulus is defined as $G^*(\omega) = G'(\omega) + iG''(\omega)$, where ω is the frequency, $G'(\omega)$ is the elastic modulus, and $G''(\omega)$ is the viscous modulus. Following Mason,[41] we used the approximation

$$\left|G^*(\omega)\right| \approx \frac{2k_BT}{3\pi a\left\langle \Delta r^2\left(\frac{1}{\omega}\right)\right\rangle \Gamma(1+\alpha(\omega))} \quad (1)$$

where k_B is the Boltzmann constant, T is the absolute temperature, a is the radius of the probe particle, Γ is the Gamma function, and

$$\alpha(\omega) = \frac{d(\ln(\Delta r^2(t))}{d(\ln(t))},\ t = \frac{1}{\omega} \quad (2)$$

is the logarithmic slope of the msd.

TEM Sample Preparation. After nTMBs were formed in the microchannel, we collected the sample and diluted the solution

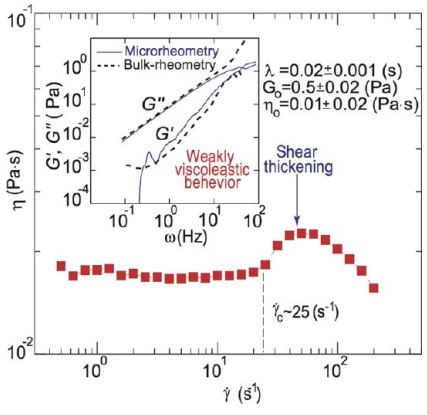

Figure 9. Shear viscosity *versus* shear rate of the precursor. The inset shows the linear viscoelastic behavior of the precursor; the dashed black line is the bulk rheometry of the precursor, while the solid blue line belongs to the microrheometry of the precursor. From the microrheometry, we obtained the relaxation time (λ = 0.02 ± 0.001 s) and plateau elastic modulus (G_0 = 0.5 ± 0.02 Pa) of the precursor. We used the bulk shear rheology to obtain the zero shear viscosity (η_0 = 0.01 ± 0.02 Pa·s) of the precursor.

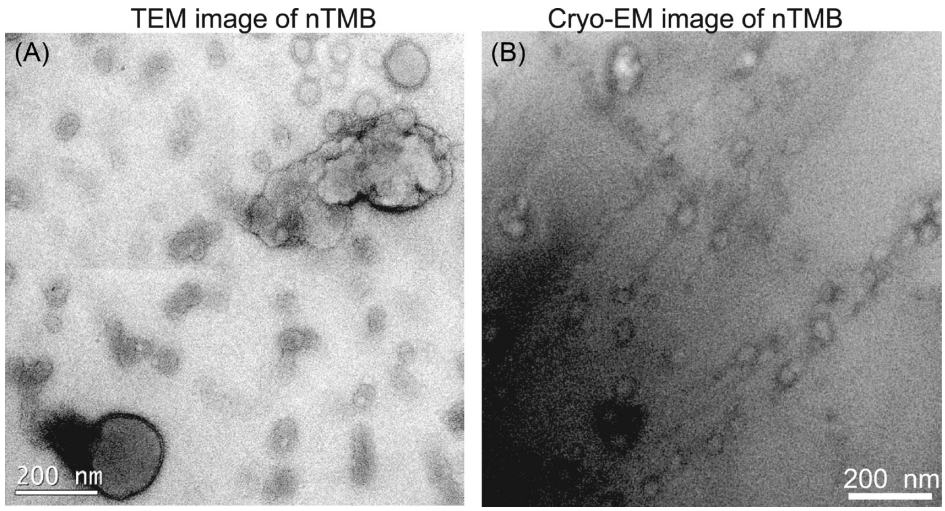

Figure 10. (A) TEM image of the nTMB with negative stain NanoW. (B) Cryo-EM images of the nTMB without negative stains.

25 times by using DI water to remove the remaining precursor, prior to TEM analysis. Most TEM samples were imaged by the Tecnai F20 transmission electron microscope (FEI Co., Hillsboro, OR) at 200 kV and equipped with a field emission gun (model Tecnai F20G2, FEI). Images were recorded under low dose conditions at a magnification of 50 000 and a pixel spacing of 2.2 Å on a 4k CCD camera (4k Eagle Camera, FEI). Some additional TEM imaging was carried out by Tecnai T-12 transmission electron microscope (FEI) at 120 kV with a LaB6 filament, coupled with a 2 × 2 K CCD camera (Gatan). TEM grids (Cu-400 mesh, Electron Microscopy Sciences, Hatfield, PA) were placed on a freshly opened holder covered with the precursor, prestrained precursor, or postflow samples. After 30 s, a 5 μL drop of the NanoW negative stain (Nanoprobes, Inc., Yaphank, NY) was applied on the material side to enhance imaging contrast. After another 30 s, the residual liquid was blotted off with a filter paper and left to air-dry.

Negative Stain for TEM Samples. Since the carbon and other light-element-based makeup in CTAB/NaSal samples has very low electron density, we employed a negative staining procedure with NanoW to enhance imaging contrast for the regular TEM imaging.[13]

One major concern about TEM imaging with negative stain is that the drying and negative staining artifacts can induce the formation of curved fringes,[44,45] which can mask the true structure of the sample. Talmon[43] and Kilpatrick *et al.*[44] observed the formation of curved fringes in surfactant solutions that were stained with uranyl acetate (UA). They concluded that the pH difference between the negative stain (UA) and the surfactant solution induced curved fringed patterns. Talmon[43] studied the mixture of "double-tailed" anionic surfactant sodium 4-(l′-heptylnonyl)benzenesulfonate (SHBS) (0.7%) with UA (1%) and reported the formation of ring-like structures. In the same work, Talmon[43] captured the formation of onion-like structures in the surfactant sodium octane (NaOct 1%) stained with 1% of UA. However, Kilpatrick *et al.* did not observe any distinct ring-like or torus-shaped structures. Instead, they observed solid-like spheres (see Figure 7 and Figure 9 in Kilpatrick *et al.*[44]). More recently, Partha *et al.*[45] reported the formation of supramolecular structures in the amphiphilic fullerene monomer (AF-I) stained with UA. They reported the formation of "buckyball", unilamellar, and multilamellar structures when the temperature and pH of the AF-I solution and UA were varied. However, they did not observe regular and well-defined ring-like structures resembling nTMB.

These well-known artifacts derived from using UA is a base for our effort of staying away from the acidic UA and identifying a proper negative stain. NanoW is an inert angstrom-range solution with organo-tungstate compound that does not react with our precursor (NaSal/CTAB) micellar solution. In addition, NanoW has chemical structure, pH, and compounds very different from those of UA. The pH of NanoW is 6.8,[13] while the pH of the nTMB sample for TEM imaging before and after adding NanoW was measured to be 6.7 ± 0.2, indicating that NanoW did not cause any major pH changes in the system. In addition, the drying artifact related to regular TEM does not provide sufficient energy to close the micellar bundles for forming the ring-structured nTMB.

Cryo-EM Sample Preparation. Cryo-EM samples were imaged by the Tecnai G2 F20 transmission electron microscope (FEI Co., Hillsboro, OR) at 200 kV and equipped with a field emission gun. Images were recorded under low-dose conditions (20 e/Å^2) at a magnification of 50 000 and a pixel spacing of 2.2 Å on a Gatan camera (Gatan, Inc., Pleasanton, CA). The freeze-plunging method was used for the material cryo-immobilization. Approximately 5 μL of the sample was applied on freshly Quanti-foil R-2/2 grids (Electron Microscopy Sciences, Hatfield, PA). The sample was allowed to adhere to the grids for 30 s before being blotted on a filter paper to remove excess solution. The sample was then immediately plunge-frozen by immersing into a reservoir with liquid ethane cooled by liquid nitrogen. The grids with the frozen sample were transferred under liquid nitrogen to the Gatan 626 cryo-holder (Gatan, Inc., Pleasanton, CA), using the cryo-transfer station. After inserting the cryo-holder to the transmission electron microscope, the temperature was maintained below ∼−178 °C at all times during the cryo-imaging.

Figure 10 shows a side-by-side comparison of nTMB images obtained from regular TEM with the negative stain and the cryo-EM without any negative stain. Based on the TEM images, the radius of the nTMBs ranges between 16 and 198 nm, with the dominant size between 30 and 40 nm (see Figure 6D) and a thickness of ∼24 ± 9 nm. Hence, the diameter and thickness dimensions of nTMBs are pretty consistent between the cryo-EM and TEM images. We did observe that nTMB structures obtained from TEM exhibited more spherical shape with a broader radius range when compared with the cryo-EM nTMB structures. The freeze-plunging method used for cryo-EM sample preparation introduced more shear in comparison to the simple blotting method for the regular TEM sample preparation, leading to slightly more elongated structures from cryo-EM. This tendency can be clearly seen in Figure 10. Nevertheless, from the morphological comparison of gradually air-dried (image A) and frozen but hydrated (image B) samples by TEM and cryo-EM, we found excellent ultrastructural correlation in both methods.

Conflict of Interest: The authors declare no competing financial interest.

Acknowledgment. We acknowledge support from the National Science Foundation (CBET 0852471 (A.Q.S.), DMR 0907638 (A.Q.S.), and DMR 0944772 (D.C.P.)). We also thank NIST, U.S. Department of Commerce, in providing access to neutron research

facilities. A portion of the research was performed using EMSL, a national scientific user facility sponsored by the Department of Energy's Office of Biological and Environmental Research and located at Pacific Northwest National Laboratory (PNNL-EMSL-39946). J.J.C. is grateful for a CONACYT-Ph.D. fellowship.

REFERENCES AND NOTES

1. Zhang, J.; Li, X.; Li, X. Stimuli-Triggered Structural Engineering of Synthetic and Biological Polymeric Assemblies. *Prog. Polym. Sci.* **2012**, *37*, 1130–1176.
2. Conwell, C. C.; Vilfan, I. D.; Hud, N. V. Controlling the Size of Nanoscale Toroidal DNA Condensates with Static Curvature and Ionic Strength. *Proc. Natl. Acad. Sci. U.S.A.* **2003**, *100*, 9296–9301.
3. Lu, Y.; Fan, H.; Stump, A.; Ward, T. L.; Rieker, T.; Brinker, J. Biomimetic Molecular Assemblies on Glass and Mesoporous Silica Microbeads for Biotechnology. *Nature* **1999**, *938*, 223–226.
4. Whitesides, G. M.; Grzybowski, B. Self-Assembly at All Scales. *Science* **2002**, *295*, 2418–2421.
5. In, M.; Aguerre-Chariol, O.; Zana, R. Closed-Looped Micelles in Surfactant Tetramer Solutions. *J. Phys. Chem. B* **1999**, *103*, 7747–7750.
6. Jain, S.; Bates, F. S. On the Origins of Morphological Complexity in Block Copolymer Surfactants. *Science* **2003**, *300*, 460–464.
7. Pochan, D. J.; Chen, Z.; Cui, H.; Hales, K.; Qi, K.; Wooley, K. L. Toroidal Triblock Copolymer Assemblies. *Science* **2004**, *306*, 94–97.
8. Shoji, O.; Tanaka, H.; Kawai, T.; Kobuke, Y. Single Molecule Visualization of Coordination-Assembled Porphyrin Macrocycles Reinforced with Covalent Linkings. *J. Am. Chem. Soc.* **2005**, *127*, 8598–8599.
9. Nie, Z. H.; Fava, D.; Kumacheva, E.; Zou, S.; Walker, G. C.; Rubinstein, M. Self-Assembly of Metal−Polymer Analogues of Amphiphilic Triblock Copolymers. *Nat. Mater.* **2007**, *6*, 609–614.
10. Wang, B.; Shum, H. C.; Weitz, D. A. Fabrication of Monodisperse Toroidal Particles by Polymer Solidification in Microfluidics. *ChemPhysChem* **2009**, *10*, 641–645.
11. Cates, M. E.; Candau, S. J. Statics and Dynamics of Wormlike Surfactant Micelles. *J. Phys.: Condens. Matter* **1990**, *74*, 6869–6891.
12. Berret, J.-F. *Molecular Gels* **2006**, Part 6, 667−720.
13. www.nanoprobes.com/pdf/Inf2018.pdf.
14. Clausen, T. M.; Vinson, P. K.; Minter, J. R.; Davis, H. T.; Ylamon, Y.; Miller, W. G. Viscoelastic Micellar Solutions: Microscopy and Rheology. *J. Phys. Chem.* **1992**, *96*, 474–484.
15. Gummel, J.; Sztucki, M.; Narayanan, T.; Gradzielskib, M. Concentration Dependent Pathways in Spontaneous Self-Assembly of Unilamellar Vesicles. *Soft Matter* **2011**, *7*, 5731–5738.
16. Cates, M. E.; Candau, S. J. Ring-Driven Shear Thickening in Wormlike Micelles? *Europhys. Lett.* **2001**, *55*, 887–893.
17. Padding, J. T.; Boek, E. S. Influence of Shear Flow on the Formation of Rings in Wormlike Micelles: A Nonequilibrium Molecular Dynamics Study. *Phys. Rev. E* **2004**, *70*, 031502–031502.
18. Helfrich, W. Elastic Properties of Lipid Bilayers: Theory and Possible Experiments. *Z. Naturforsch. C* **1973**, *28*, 693–703.
19. Iwataki, T.; Kidoaki, S.; Sakaue, T.; Yoshikawa, K.; Abramchuk, S. S Competition between Compaction of Single Chains and Bundling of Multiple Chains in Giant DNA Molecules. *J. Chem. Phys.* **2004**, *120*, 6299–6304.
20. Seifert, U. Vesicles of Toroidal Topology. *Phys. Rev. Lett.* **1991**, *66*, 2404–2407.
21. Ou-Yang, Z. C. Anchoring Ring-Vesicle Membranes. *Phys. Rev. A* **1990**, *41*, 4517–4520.
22. He, X.; Schmid, F. Spontaneous Formation of Complex Micelles from a Homogeneous Solution. *Phys. Rev. Lett.* **2008**, *100*, 137802–137802.
23. Cardiel, J. J.; Dohnalkova, A.; Dubash, N.; Zhao, Y.; Cheung, P.; Shen, A. Q. Microstructure and Rheology of a Flow-Induced Structured Phase in Wormlike Micellar Solutions. *Proc. Natl. Acad. Sci. U.S.A.* **2013**, *110*, E1653.
24. Pope, S. B. *Turbulent Flows*; Cambridge University Press: Cambridge, UK, 2000.
25. James, D. F.; McLaren, D. R. The Laminar Flow of Dilute Polymer Solutions through Porous Media. *J. Fluid Mech.* **1975**, *70*, 732–752.
26. Wang, Z.; Larson, R. Molecular Dynamics Simulations of Threadlike Cetyltrimethylammonium Chloride Micelles: Effects of Sodium Chloride and Sodium Salicylate Salts. *J. Phys. Chem. B* **2009**, *113*, 13697–13710.
27. Mohanty, S.; Davis, H. T.; McCormick, A. V. Complementary Use of Simulations and Free Energy Models for CTAB/NaSal Systems. *Langmuir* **2001**, *17*, 7160–7171.
28. Barentin, C.; Liu, A. J. Shear Thickening in Dilute Solutions of Wormlike Micelles. *Europhys. Lett.* **2001**, *55*, 432–438.
29. Jung, H. T.; Coldren, B.; Zasadzinski, J. A.; Iampietro, D. J.; Kaler, E. W. The Origins of Stability of Spontaneous Vesicles. *Proc. Natl. Acad. Sci. U.S.A.* **2001**, *98*, 1353–1357.
30. Barker, J. G.; Glinka, C. J.; Moyer, J. J.; Kim, M. H.; Drews, A. R.; Agamalian, M. Design and Performance of a Thermal-Neutron Double-Crystal Diffractometer for USANS at NIST. *J. Appl. Crystallogr.* **2005**, *38*, 1004–1011.
31. Kline, S. R. Reduction and Analysis of SANS and USANS Data Using IGOR Pro. *J. Appl. Crystallogr.* **2006**, *39*, 895–900.
32. Michalet, X.; Bensimon, D. Vesicles of Toroidal Topology: Observed Morphology and Shape Transformations. *J. Phys. II* **1995**, *5*, 263–287.
33. Helfand, E.; Fredrickson, G. H. Large Fluctuations in Polymer Solutions under Shear. *Phys. Rev. Lett.* **1989**, *62*, 2468–2471.
34. Kadoma, I. A.; Egmond, J. W. Flow-Induced Nematic String Phase in Semidilute Wormlike Micelle Solutions. *Phys. Rev. Lett.* **1998**, *80*, 5679–5682.
35. Vasudevan, M.; Buse, B.; Lu, D. L.; Krishna, H.; Kalyanaraman, R.; Shen, A. Q.; Khomami, B.; Sureshkumar, R. Irreversible Nanogel Formation in Surfactant Solutions by Microporous Flow. *Nat. Mater.* **2010**, *9*, 436–441.
36. Drye, T. J.; Cates, M. E. Living Networks: The Role of Cross-Links in Entangled Surfactant Solutions. *J. Chem. Phys.* **1992**, *96*, 1367–1375.
37. Diat, O.; Roux, D.; Nallet, F. Effect of Shear on a Lyotropic Lamellar Phase. *J. Phys. II* **1993**, *3*, 1427–1452.
38. Yusof, N. S. M.; Ashokkumar, M. Ultrasound-Induced Formation of High and Low Viscoelastic Nanostructures of Micelles. *Soft Matter* **2013**, *9*, 1997–2002.
39. Xia, Y.; Whitesides, G. M. Soft Lithography. *Annu. Rev. Mater. Sci.* **1998**, *28*, 153–184.
40. Manson, T. G.; Ganesan, K.; van Zanten, J. F.; Wirtz, D.; Kuo, S. C. Particle Tracking Microrheology of Complex Fluids. *Phys. Rev. Lett.* **1997**, *79*, 3282–3285.
41. Manson, T. G. Estimating the Viscoelastic Moduli of Complex Fluids Using the Generalized Stokes−Einstein Equation. *Rheol. Acta* **2000**, *39*, 371–378.
42. Squires, T. M.; Manson, T. G. Fluid Mechanics of Microrheology. *Annu. Rev. Fluid Mech.* **2010**, *42*, 413–438.
43. Talmon, Y. Staining and Drying-Induced Artifacts in Electron Microscopy of Surfactant Dispersions. *J. Colloid Interface Sci.* **1983**, *93*, 366–382.
44. Kilpatrick, P. K.; Miller, W. G.; Talmon, Y. Staining and Drying-Induced Artifacts in Electron Microscopy of Surfactant Dispersions. II. Change in Phase Behavior Produced by Variation in pH Modifiers, Stain, and Concentration. *J. Colloid Interface Sci.* **1985**, *107*, 146–158.
45. Partha, R.; Lackey, M.; Hirsch, A.; Casscells-Ward, S.; Conyers, J. L. Self Assembly of Amphiphilic C60 Fullerene Derivatives into Nanoscale Supramolecular Structures. *J. Nanobiotechnol.* **2007**, *5*, 1–11.
46. van Zanten, R.; Zasadzinski, J. Using Cryo-Electron Microscopy To Determine Thermodynamic and Elastic Properties of Membranes. *Curr. Opin. Colloid Interface Sci.* **2005**, *10*, 261–268.